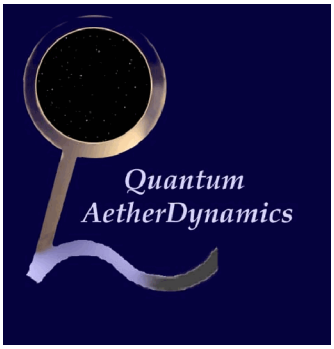

Quantum AetherDynamics Institute (QADI)

A Coupled Electron–Nuclear Periodic Law in QMU: Aether Boundary Closure and Internal Compression Quantization

David W. Thomson III
Quantum AetherDynamics Institute (QADI), Alma, Illinois, USA
ORCID: 0000-0002-5830-5427

Version 1.0 – March 12, 2026

This article is published by the Quantum AetherDynamics Institute (QADI).

It develops the Aether Physics Model (APM)

Abstract

The periodic table is traditionally interpreted as a manifestation of electron orbital filling. However, the Quantum Measurement Unit (QMU) framework and the Aether Physics Model (APM) indicate that atomic structure arises from two coupled but distinct closure conditions: (1) outer Aether boundary closure governing electron behavior, and (2) inner Aether compression closure governing nuclear stability Thomson [2025b,a]. Using the QADI Vajra and Pauling Spheron periodic tables as structural guides Thomson [2021, 2018b,a], this work formulates a coupled periodic law in QMU. The resulting framework replaces orbital-based interpretation with a discrete geometric ledger describing Aether rotation and compression. This establishes a unified basis for chemical periodicity and nuclear stability.

1 Introduction

The periodic table is one of the most successful organizing principles in science. In conventional interpretation, periodicity arises from the sequential filling of electron orbitals Royal Society of Chemistry [2026]. While this framework is operationally effective, it does not identify the physical mechanism responsible for the quantization of structure.

Within the Aether Physics Model (APM), atomic systems are not defined by orbitals, but by quantized Aether rotation and compression. The Quantum Measurement Unit (QMU) system provides a dimensional ledger in which these processes are explicitly quantified Thomson [2025b,a].

Two independent but coupled structures emerge:

1. Outer Aether boundary closure, governing chemical behavior.
2. Inner Aether compression closure, governing nuclear stability.

These structures are represented independently in the QADI periodic tables Thomson [2021]:

- The Vajra periodic table encodes the organization of the electron system as a boundary structure Thomson [2018b].
- The Pauling Spheron periodic table encodes the organization of the nucleus as a volumetric compression structure Thomson [2018a].

The objective of this paper is to formulate a periodic law that unifies these two structures within a single QMU ledger.

2 Foundational QMU Identities

The QMU system defines the fundamental geometric and dynamic quantities of Aether Thomson [2025b,a]:

$$\text{volm} = {\lambda_C}^3 \tag{1}$$

$$\text{rson} = {F_q}^2 \tag{2}$$

$$\text{curl} = \frac{{e_{\text{emax}}}^2}{m_e \lambda_C} \tag{3}$$

The Aether unit establishes the rotational–torsional closure condition:

$$A_u \cdot \text{curl} = {F_q}^2 {\lambda_C}^2 \tag{4}$$

Recognizing that $F_q \lambda_C = c$, this becomes:

$$A_u \cdot \text{curl} = c^2 \tag{5}$$

This identity represents the Aether rotational self-consistency condition and forms the basis for all closure behavior.

Potential (potn) admits multiple equivalent QMU identities:

$$\text{potn} = \frac{A_u}{\text{leng}} = \text{indc} \cdot \text{rson} \tag{6}$$

These relations establish that confinement, rotation, and frequency are not independent quantities, but different projections of the same Aether state.

3 Electron Boundary Closure Law

The Vajra periodic table reveals that atomic structure is organized into discrete band systems. Each shell begins with a two-state boundary, terminates in a six-state closure, and may include intermediate bands increasing in even increments Thomson [2018b].

Define the shell band set:

$$\mathcal{B}_\mu = \{2\} \cup \{8, 10, 12, \ldots, 2\mu + 6\} \cup \{6\} \tag{7}$$

The total boundary capacity for a shell is:

$$E_\mu = 2 + 6 + \sum_{k=0}^{\mu-1} (8 + 2k) \tag{8}$$

For $\mu \geq 0$, this reduces to:

$$E_\mu = \mu^2 + 7\mu + 8 \tag{9}$$

with the base case:

$$E_{-1} = 2 \tag{10}$$

This sequence defines the allowed Aether boundary closures for atomic systems.

The electron periodic law is therefore a discrete geometric closure condition:

$$\Gamma_e = E_\mu \tag{11}$$

Each element occupies a position within $\mathcal{B}_\mu$, corresponding to a specific boundary topology and polarity.

The boundary-band organization underlying this law is shown in Fig. 1.

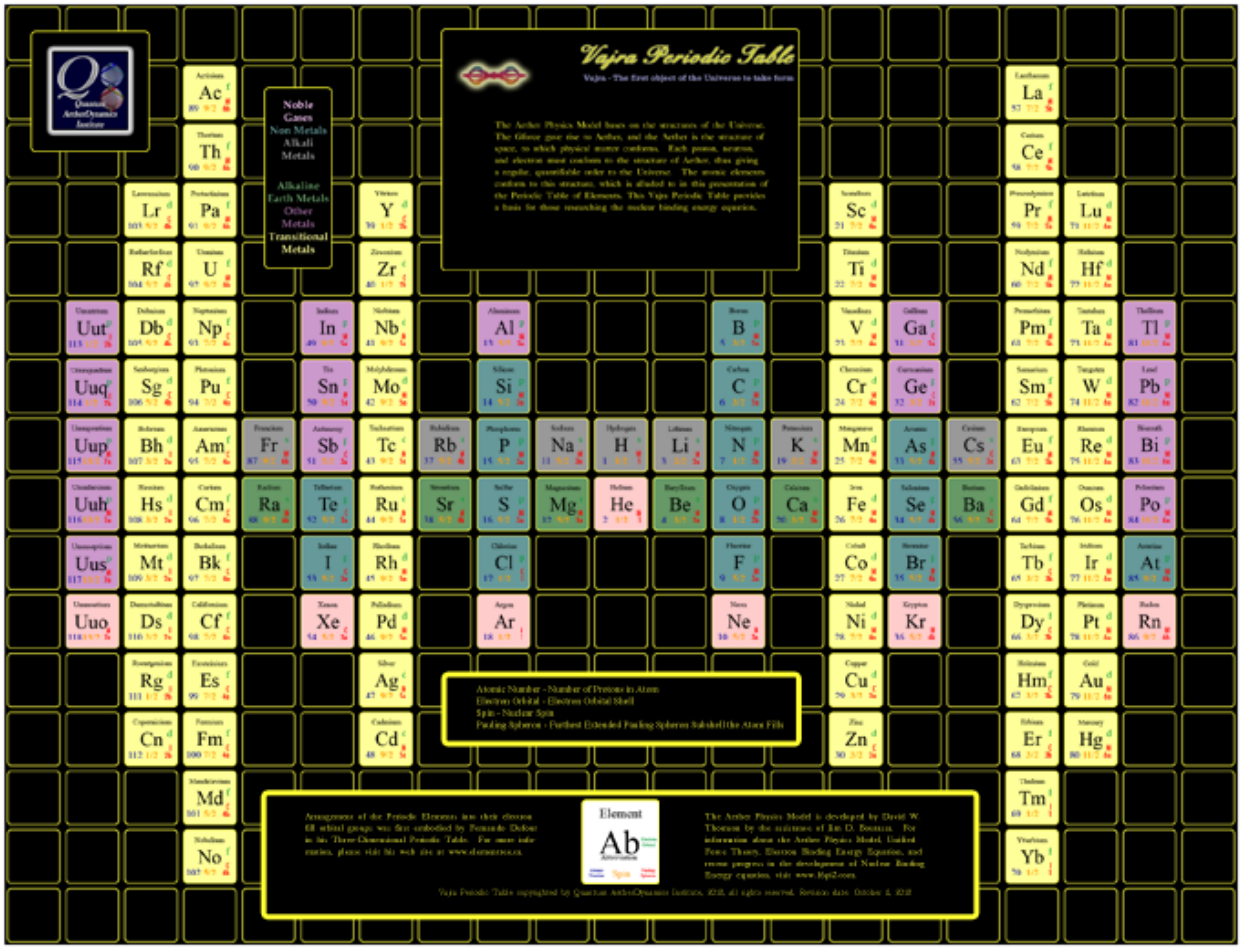

Figure 1: Vajra periodic table showing the discrete Aether boundary geometry used for the electron-side periodic law. Each shell begins with a two-space polar initiation band and terminates in a six-space closure band, with intermediate even bands representing distributed boundary layers. This structure underlies the band recursion, group-position topology, and the paired derivation of the chemical period lengths.

4 Nuclear Compression Closure Law

The Pauling Spheron periodic table reveals that the nucleus is structured as a layered compression system consisting of Thomson [2018a]:

- Mantle
- Center
- Inner Core

Dominant closure occurs at the mantle level, corresponding to the sequence:

$$\mathcal{M} = \{2, 8, 20, 28, 50, 82\} \tag{12}$$

which matches the standard magic-number sequence up to 82 for proton closures and major shell

closures more generally Thomson [2018a], Otsuka et al. [2020].

Define the nuclear closure deviation:

$$\Pi_n^{(1)}(x) = \min_{m \in \mathcal{M}} |x - m| \tag{13}$$

where x represents either proton number Z or neutron number N.

The first-order nuclear closure condition is:

$$\Gamma_n(Z, N) = \Pi_n^{(1)}(Z) + \Pi_n^{(1)}(N) \tag{14}$$

This expression quantifies the deviation from optimal Aether compression.

The layered compression structure used in the nuclear closure functional is shown in Fig. 2.

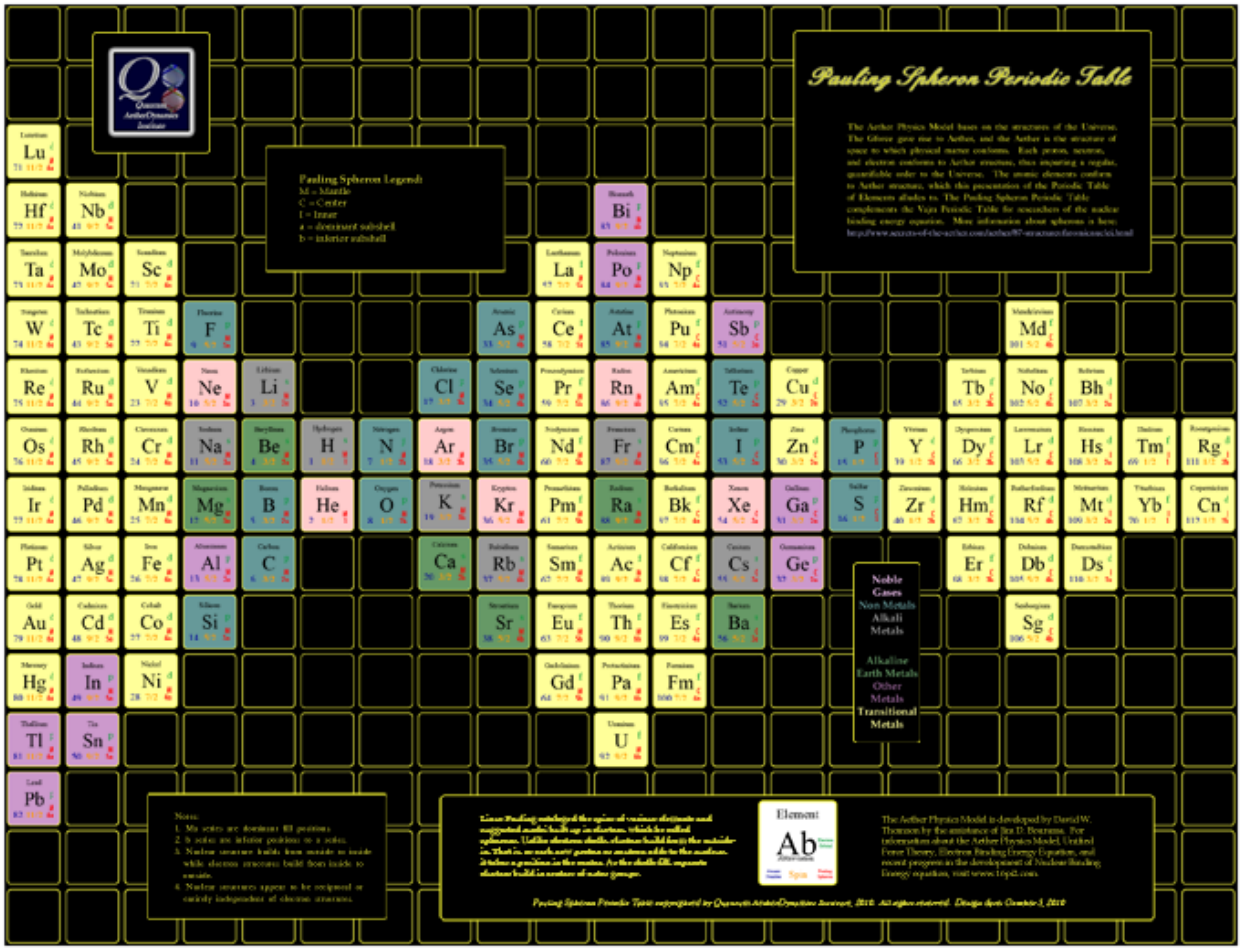

Figure 2: Pauling Spheron periodic table showing the nuclear compression geometry used for the nuclear-side periodic law. The mantle, center, and inner-core regions define layered compression structure, while the mantle closures at 2, 8, 20, 28, 50, and 82 correspond to the dominant magic-number sequence used in the first-order nuclear closure functional.

5 Coupled Periodic Law

The full periodic behavior arises from the coupling of boundary and compression closures.

Define the total periodic functional:

$$\Pi(Z, N; \mu) = \alpha \, |Z - \Gamma_e(\mu)| + \beta \, \Gamma_n(Z, N) \tag{15}$$

where α and β weight boundary and compression contributions.

Weighting Regime Across Shell Order. The weighting coefficients α and β are not universal constants, but scale-dependent parameters reflecting the relative influence of boundary closure and internal compression across shell order μ. Accordingly, we write

$$\alpha = \alpha_\mu, \qquad \beta = \beta_\mu, \tag{16}$$

with the ordering

$$\alpha_\mu > \beta_\mu \quad \text{for low } \mu, \tag{17}$$

and a monotonic increase in the ratio

$$\frac{\beta_\mu}{\alpha_\mu} \uparrow \quad \text{as } \mu \text{ increases.} \tag{18}$$

A convenient parametrization consistent with the recurrence law is

$$\alpha_\mu = \alpha_0 S_\mu^{-1}, \qquad \beta_\mu = \beta_0 \, (1 + \rho_\mu) \, , \tag{19}$$

where S_μ is the shell-scaling factor introduced in the recurrence relation, and ρ_μ is a compression-enhancement factor that increases with shell order and average nuclear deviation.

Thus, in the light-element regime (μ small), the periodic functional is boundary-dominated:

$$\Pi \approx \alpha_\mu |Z - \Gamma_e(\mu)|, \tag{20}$$

while in heavier systems, nuclear compression increasingly modulates the boundary:

$$\Pi \approx \alpha_\mu |Z - \Gamma_e(\mu)| + \beta_\mu \Gamma_n(Z, N), \qquad \beta_\mu / \alpha_\mu \not\ll 1. \tag{21}$$

The chemical recurrence remains governed by Γ_e, but its heavy-period distortion is progressively controlled by Γ_n.

An element is most stable or chemically distinct when:

$$\Pi \to \min \tag{22}$$

Thus, periodic behavior emerges from simultaneous minimization of:

- Aether boundary mismatch (electron structure)
- Aether compression mismatch (nuclear structure)

6 Interpretation

The periodic law may be stated succinctly:

> Atomic properties recur when Aether boundary closure and internal compression closure recur simultaneously.

This replaces the orbital-filling interpretation with a geometric Aether ledger.

7 Worked Examples

To demonstrate the predictive and interpretive capability of the coupled periodic law, representative elements are examined across distinct structural regimes. Each example is evaluated in terms of:

- Electron boundary closure: Γ_e
- Nuclear compression closure: Γ_n
- Total periodic functional: Π

7.1 Helium (He): Pure Boundary Closure

Helium ($Z = 2$, $N = 2$) represents the minimal atomic system and corresponds to the base boundary closure:

$$E_{-1} = 2 \tag{23}$$

Thus:

$$\Gamma_e = 2, \qquad Z = 2 \quad \Rightarrow \quad \text{perfect boundary closure} \tag{24}$$

For the nucleus:

$$Z = 2 \in \mathcal{M}, \qquad N = 2 \in \mathcal{M} \tag{25}$$

$$\Gamma_n = 0 \tag{26}$$

Therefore:

$$\Pi = 0 \tag{27}$$

Helium represents complete Aether closure in both boundary and compression. Its chemical inertness follows directly from the absence of boundary discontinuities:

$$\nabla(\text{curl}) = 0 \tag{28}$$

This is the simplest realization of a self-contained Aether structure.

7.2 Neon (Ne): Higher-Order Boundary Closure

Neon ($Z = 10$, $N = 10$) corresponds to the first complete shell beyond helium.

From the boundary law:

$$E_0 = 8, \quad E_1 = 16 \tag{29}$$

Neon lies at the terminal band of the $[2, 6]$ structure, giving effective closure:

$$\Gamma_e = 10 \tag{30}$$

Thus:

$$Z = \Gamma_e \quad \Rightarrow \quad \text{boundary closure satisfied} \tag{31}$$

For nuclear closure:

$$\Pi_n^{(1)}(10) = \min(|10 - 8|, |10 - 20|) = 2 \tag{32}$$

$$\Gamma_n = 2 + 2 = 4 \tag{33}$$

Thus:

$$\Pi = \beta \cdot 4 \tag{34}$$

Neon demonstrates that chemical inertness is dominated by boundary closure even when nuclear closure is not exact.

Interpretation:

> Chemical periodicity is governed primarily by Aether boundary conditions, while nuclear compression contributes secondary corrections.

7.3 Iron (Fe): Compression-Dominated Stability

Iron ($Z = 26$, $N = 30$) lies near the peak region of nuclear binding energy per nucleon Thomson [2018a], Nave [2026].

Electron boundary:

$$E_2 = 26 \tag{35}$$

$$\Gamma_e = 26, \quad Z = 26 \quad \Rightarrow \quad \text{boundary alignment} \tag{36}$$

Nuclear closure:

$$\Pi_n^{(1)}(26) = |26 - 28| = 2 \tag{37}$$

$$\Pi_n^{(1)}(30) = |30 - 28| = 2 \tag{38}$$

$$\Gamma_n = 4 \tag{39}$$

Although not exactly at a magic number, iron lies symmetrically about 28, producing a near-minimal compression deviation.

Interpretation:

> Maximum nuclear stability occurs not only at closure, but also at symmetric compression about a closure boundary.

This explains the observed peak in binding energy per nucleon near iron Nave [2026].

7.4 Xenon (Xe): Dual Closure Alignment

Xenon ($Z = 54$, $N \approx 77$) represents a heavy noble gas with near-dual closure.

Electron boundary:

$$\Gamma_e \approx 54 \quad \Rightarrow \quad \text{terminal band closure} \tag{40}$$

Nuclear closure:

$$\Pi_n^{(1)}(54) = |54 - 50| = 4 \tag{41}$$

$$\Pi_n^{(1)}(77) = |77 - 82| = 5 \tag{42}$$

$$\Gamma_n = 9 \tag{43}$$

Despite nonzero nuclear deviation, xenon exhibits strong chemical inertness due to dominant boundary closure.

Interpretation:

> As atomic number increases, boundary closure remains the primary determinant of chemical behavior, while compression deviation grows gradually.

7.5 Lead (Pb): Heavy Compression Deviation

Lead ($Z = 82$, $N = 126$) is a heavy element with strong nuclear closure but weaker boundary alignment Otsuka et al. [2020].

Nuclear closure:

$$Z = 82 \in \mathcal{M}, \qquad N = 126 \text{ (extended closure)} \tag{44}$$

$$\Gamma_n \approx 0 \tag{45}$$

Electron boundary:

$$Z = 82 \neq \Gamma_e(\mu) \quad \Rightarrow \quad \text{boundary mismatch} \tag{46}$$

Thus:

$$\Pi \approx \alpha |Z - \Gamma_e| \tag{47}$$

Interpretation:

> Heavy-element stability is dominated by internal compression closure even when boundary closure is imperfect.

This explains why lead is stable despite reduced chemical inertness.

7.6 Summary of Regimes

The worked examples reveal three dominant regimes:

1. **Boundary-dominated closure:** He, Ne, Xe
2. **Compression-dominated stability:** Fe, Pb
3. **Coupled optimization:** transitional elements near dual minima

The periodic table is therefore not governed by a single mechanism, but by the interaction of two independent Aether closure processes.

$$\text{Periodic behavior} = \text{boundary closure} + \text{compression closure} \tag{48}$$

8 Derivation of Period Lengths from QMU Geometry

The familiar period lengths of the chemical periodic table,

$$2,\ 8,\ 8,\ 18,\ 18,\ 32,\ 32, \ldots \tag{49}$$

are usually presented as empirical consequences of orbital filling. In the present framework, these lengths arise instead from a discrete Aether boundary geometry described by the Vajra periodic table Thomson [2018b].

The Vajra structure provides the required geometric rules explicitly Thomson [2018b]:

1. Each shell begins with two spaces.
2. The first shell has only two spaces.
3. Outer shells terminate with a six-space band.
4. The shell patterns progress as

$$2; \qquad 2,6; \qquad 2,8,6; \qquad 2,10,8,6; \qquad 2,12,10,8,6; \ldots$$

5. The shell architecture occurs in overlapping pairs: second and third, third and fourth, fourth and fifth, fifth and sixth, and so on.

These features show that period length is not a primitive quantity. It is a derived quantity obtained from the cumulative closure of nested Aether boundary bands.

8.1 Band Recursion

Let the shell-geometry order be indexed by μ. Define the shell-band list $\mathcal{B}_\mu$ by

$$\mathcal{B}_{-1} = (2), \tag{50}$$
$$\mathcal{B}_0 = (2, 6), \tag{51}$$
$$\mathcal{B}_1 = (2, 8, 6), \tag{52}$$
$$\mathcal{B}_2 = (2, 10, 8, 6), \tag{53}$$
$$\mathcal{B}_3 = (2, 12, 10, 8, 6), \tag{54}$$

and in general, for $\mu \geq 0$,

$$\mathcal{B}_\mu = (2,\ 2\mu + 6,\ 2\mu + 4,\ \ldots,\ 8,\ 6)\,. \tag{55}$$

Thus, beyond the initial two-space boundary, the interior bands descend by even steps until the terminal six-space closure is reached.

The total shell capacity associated with $\mathcal{B}_\mu$ is

$$E_\mu = \sum_{b \in \mathcal{B}_\mu} b. \tag{56}$$

Evaluating the first cases,

$$E_{-1} = 2, \tag{57}$$
$$E_0 = 2 + 6 = 8, \tag{58}$$
$$E_1 = 2 + 8 + 6 = 16, \tag{59}$$
$$E_2 = 2 + 10 + 8 + 6 = 26, \tag{60}$$
$$E_3 = 2 + 12 + 10 + 8 + 6 = 38. \tag{61}$$

For $\mu \geq 0$, the closed form is

$$E_\mu = 2 + \sum_{k=0}^{\mu} (2k + 6) \tag{62}$$
$$= 2 + (\mu + 1)6 + 2 \sum_{k=0}^{\mu} k \tag{63}$$
$$= 2 + 6(\mu + 1) + \mu(\mu + 1) \tag{64}$$
$$= \mu^2 + 7\mu + 8. \tag{65}$$

Therefore,

$$\boxed{E_\mu = \mu^2 + 7\mu + 8 \qquad (\mu \geq 0)} \tag{66}$$

with the special base shell

$$E_{-1} = 2. \tag{67}$$

The quantities E_μ are not yet the conventional period lengths. They are the *full Aether boundary capacities* of the Vajra shell geometries.

8.2 Why the Chemical Periods Repeat in Pairs

The Vajra description shows that shell architectures repeat in overlapping adjacent shells rather than appearing only once. The second and third shells share the same outer pattern, the third and fourth share the next pattern, and this paired recurrence continues outward. This indicates that chemical periods are generated by *successive increments* in shell geometry, not by the absolute shell totals themselves Thomson [2018b].

Define the chemical period length P_n as the incremental increase in boundary capacity when a new active shell geometry appears, with each new geometry contributing to two successive periods after the first. The first period is exceptional:

$$P_1 = 2. \tag{68}$$

For the outer periods, the increment law is

$$P_{2m} = P_{2m+1} = 4m^2 + 4m + 2, \qquad m = 1, 2, 3, \ldots \tag{69}$$

This generates

$$P_2 = P_3 = 8, \tag{70}$$
$$P_4 = P_5 = 18, \tag{71}$$
$$P_6 = P_7 = 32, \tag{72}$$

which is the standard sequence.

This may also be written in the familiar form

$$\boxed{P_{2m} = P_{2m+1} = 2(m+1)^2} \qquad (m \geq 1), \tag{73}$$

with

$$P_1 = 2. \tag{74}$$

The conventional period law is therefore recovered, but here it is no longer primary. It arises from paired activation of Vajra boundary geometries.

8.3 Connection Between the Vajra Bands and the Period Law

The paired period law can be obtained directly from the band sequence.

Each shell contains:

1. a two-space polar initiation band,
2. zero or more transitional metal bands of size $8, 10, 12, \ldots$,
3. a six-space terminal nonmetal closure band.

The period length is the number of distinct Aether boundary sites that become chemically active before the next boundary symmetry closes. Because the shell architectures recur in adjacent pairs, each geometry contributes twice:

$$2 \to 8, 8 \to 18, 18 \to 32, 32 \to \cdots \tag{75}$$

Hence the familiar sequence is a *duplicated shell-increment law*. The duplication is not arbitrary; it is a direct consequence of the right-left and up-down polarity alternations built into the Vajra architecture. The table description explicitly notes both lateral and vertical polarity relations in the shell pattern Thomson [2018b].

This allows the period law to be interpreted as a polarity-balanced closure rule:

$$\boxed{\text{period length} = \text{number of allowed boundary sites before polarity-balanced closure.}} \tag{76}$$

8.4 QMU Interpretation

In QMU, the boundary structure is not an electron cloud but a discrete Aether ledger. The relevant geometric quantities are the Aether unit A_u, the rotational unit curl, and the confinement relation

$$\text{potn} = \frac{A_u}{\text{leng}}. \tag{77}$$

A closed shell corresponds to a complete boundary ledger in which the available sites of the Vajra geometry are exhausted. The period length is therefore the count of distinct boundary placements available under a given confinement scale before a new closure topology must be invoked.

Thus the period law may be written conceptually as

$$P_n = \Delta\Gamma_e, \tag{78}$$

where Γ_e is the electron-side boundary closure coordinate. In this picture:

- the two-space band sets the polar seed,
- the even transitional bands encode distributed shear layers,
- the six-space terminal band completes the chemically closed boundary.

The usual sequence

$$2,\ 8,\ 8,\ 18,\ 18,\ 32,\ 32, \ldots \tag{79}$$

is therefore the observable chemical projection of a deeper QMU recursion:

$$\mathcal{B}_{-1},\ \mathcal{B}_0,\ \mathcal{B}_1,\ \mathcal{B}_2,\ \mathcal{B}_3, \ldots \tag{80}$$

8.5 Coupling to the Nuclear Periodic Law

The derivation above applies only to the outer boundary structure. The QADI home page explicitly distinguishes this electron-side organization from the nuclear organization, which requires the Pauling Spheron table. The Spheron description identifies the Mantle, Center, and Inner Core zones and gives the magic-number mantle closures

$$2,\ 8,\ 20,\ 28,\ 50,\ 82. \tag{81}$$

These govern nuclear compression rather than chemical period length Thomson [2021, 2018a].

Accordingly, the full QMU periodic law remains coupled:

$$\Pi(Z, N; \mu) = \alpha\,|Z - \Gamma_e(\mu)| + \beta\,\Gamma_n(Z, N), \tag{82}$$

but only the first branch generates the familiar repeated chemical periods.

8.6 Result

The period lengths of the chemical periodic table are derived from the Vajra shell geometry as follows:

1. The shell bands obey the recursive sequence

$$(2),\ (2,6),\ (2,8,6),\ (2,10,8,6),\ (2,12,10,8,6),\ldots$$

2. The absolute shell capacities are

$$E_{-1} = 2, \qquad E_\mu = \mu^2 + 7\mu + 8.$$

3. The observable chemical periods arise from paired activation of successive shell geometries:

$$P_1 = 2, \qquad P_{2m} = P_{2m+1} = 2(m+1)^2.$$

Therefore, the familiar sequence

$$\boxed{2,\ 8,\ 8,\ 18,\ 18,\ 32,\ 32,\ldots} \tag{83}$$

is interpreted in APM as the discrete recurrence of polarity-balanced Aether boundary closures.

9 Group Structure from Band Position

The periodic groups (columns) are traditionally attributed to similar electron configurations. In the present framework, group behavior arises from the position of an element within the Vajra boundary band structure Thomson [2018b].

Each element occupies a specific location within a shell band set:

$$\mathcal{B}_\mu = (2,\ 2\mu + 6,\ 2\mu + 4,\ \ldots,\ 8,\ 6) \tag{84}$$

Thus, group identity is determined by *band position*, not orbital type.

Define the band-position coordinate:

$$g = (b,\ s) \tag{85}$$

where:

- b is the band size (2, 6, 8, 10, 12, ...),
- s is the polarity position (left/right or up/down orientation).

Chemical similarity arises when elements share the same (b, s) across different shells.

9.1 Polar Initiation Band (b = 2)

The first band in every shell is the two-space polar band:

$$b = 2 \tag{86}$$

This band corresponds to the alkali-metal group.

Properties:

- Single boundary discontinuity
- Maximum outward Aether gradient
- Strong tendency toward boundary completion

In QMU terms, this corresponds to a maximal imbalance in the boundary potential gradient:

$$\nabla(\text{potn}) \text{ large} \tag{87}$$

This explains:

- High reactivity
- Low ionization energy

9.2 Secondary Polar Band (b = 2, opposite polarity)

The second position in the two-band structure corresponds to the alkaline-earth metals.

Properties:

- Partial boundary stabilization
- Reduced gradient compared to alkali metals
- Still strongly reactive

Interpretation:

$$\nabla(\text{potn}) \text{ reduced but nonzero} \tag{88}$$

9.3 Transitional Bands (b = 8, 10, 12, . . .)

Intermediate bands correspond to the transition metals and related groups:

$$b = 8,\ 10,\ 12,\ \ldots \tag{89}$$

These bands represent distributed boundary layers within the Aether structure.

Properties:

- Multiple allowable boundary configurations
- Variable oxidation states
- Strong coupling between boundary and interior

In QMU:

$$\text{potn} = \text{freq} \cdot \text{mflx} \tag{90}$$

This indicates that potential is dynamically distributed across the boundary, rather than concentrated at a single discontinuity.

Interpretation:

> Transitional bands are shear layers in the Aether boundary, permitting multiple stable configurations.

This explains:

- Catalytic behavior
- Magnetic properties
- Electronic variability

9.4 Terminal Closure Band (b = 6)

The final band in each shell is the six-space closure band:

$$b = 6 \tag{91}$$

This corresponds to the nonmetal and noble gas groups.

Properties:

- Complete boundary closure
- Minimal external Aether gradient
- Chemical inertness (noble gases)

The closure condition is:

$$\nabla(\text{curl}) = 0 \tag{92}$$

This is equivalent to the Aether self-consistency condition:

$$A_u \cdot \mathrm{curl} = c^2 \tag{93}$$

Interpretation:

> The terminal band represents a closed Aether boundary with no residual discontinuity.

9.5 Polarity Structure

The Vajra table explicitly encodes polarity in two directions Thomson [2018b]:

- Right–left polarity (charge asymmetry)
- Up–down polarity (shell recursion)

Thus, two elements may share the same band size b but differ in polarity coordinate s.

Define:

$$g = (b, s_\ell, s_v) \tag{94}$$

where:

- s_ℓ is lateral polarity,
- s_v is vertical (shell) polarity.

This explains:

- Diagonal relationships in the periodic table
- Variations within a group
- Differences between light and heavy analogs

9.6 Group Law

Group behavior is therefore governed by invariance of band position:

$$\boxed{\text{Group identity } \equiv \ (b, s) \text{ invariant across shells}} \tag{95}$$

This replaces the conventional statement:

> "Elements in the same group have similar valence electron configurations."

with the QMU statement:

> Elements in the same group occupy equivalent Aether boundary positions within successive shell geometries.

9.7 Connection to Period Law

The period law derived previously determines how many boundary positions exist in a given shell:

$$P_n = \Delta\Gamma_e \tag{96}$$

The group law determines how those positions are organized:

$$\Gamma_e \to (b, s) \tag{97}$$

Thus:

$$\text{Periodic table} = (\text{number of boundary sites}) + (\text{organization of boundary sites}) \tag{98}$$

9.8 Result

The periodic groups arise directly from the Vajra band structure:

1. $b = 2$ bands $\to$ alkali and alkaline-earth groups
2. $b = 8, 10, 12, \ldots$ bands $\to$ transition and inner-transition groups
3. $b = 6$ band $\to$ nonmetals and noble gases

Therefore, chemical group behavior is a manifestation of Aether boundary topology rather than electron configuration.

$$\boxed{\text{Chemical similarity} = \text{shared boundary topology in QMU}} \tag{99}$$

10 Quantitative Mapping of Ionization Energy and non-bonded atomic radius

The preceding sections establish that periodic behavior arises from discrete Aether boundary closure. To elevate the framework from structural to predictive, measurable quantities must be mapped to QMU coordinates.

Two primary observables are considered:

- Ionization energy (IE)
- non-bonded atomic radius (R)

These correspond respectively to:

- Boundary disruption energy
- Boundary confinement scale

10.1 Non-bonded Atomic Radius as Aether Length Scale

In QMU, confinement is expressed through the potential relation:

$$\text{potn} = \frac{A_u}{\text{leng}} \tag{100}$$

Solving for length:

$$\text{leng} = \frac{A_u}{\text{potn}} \tag{101}$$

We identify the non-bonded atomic radius with the boundary length scale up to a band-dependent geometric factor:

$$R = \kappa_b \, \text{leng} \tag{102}$$

Thus:

$$\boxed{R \propto \kappa_b \frac{A_u}{\text{potn}}} \tag{103}$$

The factor κ_b accounts for band-dependent geometry of the outer boundary. This is especially relevant when comparing terminal closure bands, polar initiation bands, and transition-metal shear bands, since the measured non-bonded radius is not expected to be a perfect one-to-one map of the underlying QMU length.

This immediately predicts:

- Across a period: potn increases $\Rightarrow$ R decreases
- Down a group: effective potn decreases $\Rightarrow$ R increases

This reproduces the known periodic radius trends Royal Society of Chemistry [2026], Alvarez [2013].

10.2 Ionization Energy as Boundary Disruption

Ionization corresponds to breaking the outer Aether boundary closure.

Using the QMU identity:

$$\text{potn} = \text{indc} \cdot \text{rson} \tag{104}$$

and recalling:

$$\text{rson} = {F_q}^2 \tag{105}$$

we identify ionization energy as proportional to the boundary potential:

$$\boxed{\text{IE} \propto \text{potn}} \tag{106}$$

Combining with the radius relation gives

$$\text{IE} \propto \frac{\kappa_b A_u}{R} \tag{107}$$

or equivalently,

$$\boxed{\text{IE} \propto \frac{A_u}{R}} \tag{108}$$

with the geometric factor absorbed into the band dependence. This is the central quantitative prediction.

10.3 Discrete Band Correction

The continuous scaling above is modified by discrete band position.

Define the band index:

$$b \in \{2, 6, 8, 10, 12, \dots\} \tag{109}$$

Introduce a band factor C_b representing boundary topology:

$$\text{IE} = C_b \cdot \frac{A_u}{R} \tag{110}$$

with:

- C_b large for terminal closure band ($b = 6$)
- C_b small for polar initiation band ($b = 2$)
- C_b intermediate and variable for transition bands

Thus:

$$\boxed{\mathrm{IE}(Z) = C_b(Z)\,\frac{A_u}{R(Z)}} \tag{111}$$

This explains:

- Low IE of alkali metals ($b = 2$)
- High IE of noble gases ($b = 6$)
- Irregular IE of transition metals

10.4 QMU Normalization

Define a dimensionless ionization parameter:

$$\eta = \frac{\mathrm{IE} \cdot R}{A_u} \tag{112}$$

Thus:

$$\boxed{\eta = C_b} \tag{113}$$

This predicts that:

- Elements in the same group share similar η
- Deviations arise from nuclear compression effects

More strongly, the reduced measurable

$$\eta^* = \mathrm{IE} \cdot R \tag{114}$$

is expected to scale directly with the Aether unit itself:

$$\eta^* \sim A_u\, C_b \tag{115}$$

Therefore, η^* is not merely a proxy for closure. It is a direct experimental measure of Aether-unit modulation by boundary topology.

Using the QMU closure identity

$$A_u \cdot \mathrm{curl} = c^2 \tag{116}$$

with

$$\text{curl} = \frac{{e_{\text{emax}}}^2}{m_e \lambda_C}, \tag{117}$$

the Aether unit may be written as

$$A_u = \frac{c^2}{\text{curl}} = \frac{c^2 m_e \lambda_C}{{e_{\text{emax}}}^2}. \tag{118}$$

Hence the reduced ionization parameter admits the constant bridge

$$\boxed{\eta^* \sim \frac{c^2 m_e \lambda_C}{{e_{\text{emax}}}^2} C_b} \tag{119}$$

Thus, measured ionization data provide a direct experimental probe of the Aether unit expressed in fundamental constants, while the discrete variation of η^* across elements reflects modulation of this base scale by boundary topology.

This provides a direct experimental test and an explicit bridge from the periodic data to the QMU base system.

10.5 Nuclear Correction Term

The nuclear contribution enters through the compression deviation:

$$\Gamma_n(Z, N) \tag{120}$$

Introduce a correction:

$$\text{IE} = C_b \frac{A_u}{R} (1 + \epsilon \Gamma_n) \tag{121}$$

where ϵ is a small coupling parameter.

This predicts:

- Slight IE shifts across isotopes
- Enhanced stability near nuclear closure
- Anomalies in heavy elements

Two regimes are then distinguished naturally:

$$\Gamma_n \ll \Gamma_e \qquad \text{electron-dominated regime} \tag{122}$$

$$\Gamma_n \sim \Gamma_e \qquad \text{heavy-element coupled regime} \tag{123}$$

In the first regime, boundary topology dominates the observable ionization behavior. In the second, internal compression increasingly distorts the boundary closure and produces heavier-element departures from ideal shell recurrence.

10.6 Scaling Across Periods

Using the period law:

$$P_{2m} = P_{2m+1} = 2(m+1)^2 \tag{124}$$

the radius scaling may be approximated as:

$$R \sim \frac{1}{m} \tag{125}$$

Thus:

$$\text{IE} \sim m \tag{126}$$

This explains the general increase of ionization energy across periods.

10.7 Experimental Program

The QMU mapping yields direct testable predictions:

1. Plot $\eta = \text{IE} \cdot R/A_u$ across elements
2. Group clustering should appear by band index b
3. Transition metals should show spread due to shear-layer behavior
4. Noble gases should maximize η

A second test:

1. Compare isotopic IE variations with Γ_n
2. Look for correlation with magic-number proximity

10.8 Result

The primary quantitative relations are:

$$R \propto \frac{A_u}{\text{potn}} \tag{127}$$

$$\text{IE} \propto \text{potn} \tag{128}$$

$$\text{IE} \propto \frac{A_u}{R} \tag{129}$$

$$\eta = \frac{\text{IE} \cdot R}{A_u} = C_b \tag{130}$$

These establish that:

Ionization energy and non-bonded atomic radius are dual measures of Aether boundary curvature, modulated by discrete band topology.

11 Numerical Evaluation of the QMU Ionization Parameter

Using measured first ionization energies from the NIST Atomic Spectra Database and non-bonded atomic-radius values from the Royal Society of Chemistry periodic-table database, with the radius choice understood as a non-bonded/vdW-style boundary proxy Kramida et al. [2024], Royal Society of Chemistry [2026], Alvarez [2013], the QMU ionization parameter becomes experimentally testable.

Using the QMU definition

$$\eta = \frac{\mathrm{IE} \cdot R}{A_u}, \tag{131}$$

where IE is the first ionization energy and R is the non-bonded atomic radius, the factor A_u is constant for all elements. Therefore, the observable ordering is captured by the reduced parameter

$$\eta^* \equiv \mathrm{IE} \cdot R. \tag{132}$$

For the present first-order test, the following quantities are used:

- First ionization energy from critically evaluated atomic data
- Non-bonded atomic radius as the boundary-length proxy

This gives a consistent first comparison across the worked-example elements.

Using the QMU definition

$$\eta = \frac{\mathrm{IE} \cdot R}{A_u}, \tag{133}$$

where IE is the first ionization energy and R is the atomic non-bonded atomic radius, the factor A_u is constant for all elements. Therefore, the observable ordering is captured by the reduced parameter

$$\eta^* \equiv \mathrm{IE} \cdot R. \tag{134}$$

For the present first-order test, the following quantities are used:

- First ionization energy from critically evaluated atomic data
- Non-bonded atomic radius as the boundary-length proxy

This gives a consistent first comparison across the worked-example elements.

11.1 Reference Data

For helium, neon, iron, xenon, and lead, the adopted values are Kramida et al. [2024], Royal Society of Chemistry [2026]:

$$\text{He}: \quad \text{IE} = 24.587389 \text{ eV}, \qquad R = 1.400 \text{ Å} \tag{135}$$
$$\text{Ne}: \quad \text{IE} = 21.56454 \text{ eV}, \qquad R = 1.54 \text{ Å} \tag{136}$$
$$\text{Fe}: \quad \text{IE} = 7.9024 \text{ eV}, \qquad R = 2.04 \text{ Å} \tag{137}$$
$$\text{Xe}: \quad \text{IE} = 12.1298437 \text{ eV}, \qquad R = 2.16 \text{ Å} \tag{138}$$
$$\text{Pb}: \quad \text{IE} = 7.4166799 \text{ eV}, \qquad R = 2.02 \text{ Å} \tag{139}$$

The corresponding reduced ionization parameters are:

$$\eta^*_{\text{He}} = 24.587389 \times 1.400 = 34.42 \tag{140}$$
$$\eta^*_{\text{Ne}} = 21.56454 \times 1.54 = 33.21 \tag{141}$$
$$\eta^*_{\text{Fe}} = 7.9024 \times 2.04 = 16.12 \tag{142}$$
$$\eta^*_{\text{Xe}} = 12.1298437 \times 2.16 = 26.20 \tag{143}$$
$$\eta^*_{\text{Pb}} = 7.4166799 \times 2.02 = 14.98 \tag{144}$$

11.2 Tabulated Results

Table 1: Reduced QMU ionization parameter for representative elements.

Element	Z	IE (eV)	R (Å)	$\eta^* = \text{IE} \cdot R$
He	2	24.5873890	1.400	34.42
Ne	10	21.56454	1.54	33.21
Fe	26	7.9024	2.04	16.12
Xe	54	12.1298437	2.16	26.20
Pb	82	7.4166799	2.02	14.98

11.3 Interpretation by Boundary Topology

The numerical ordering is immediately suggestive:

$$\eta^*_{\text{He}} \approx \eta^*_{\text{Ne}} > \eta^*_{\text{Xe}} \gg \eta^*_{\text{Fe}} \gtrsim \eta^*_{\text{Pb}} \tag{145}$$

This supports the QMU interpretation that chemically closed boundaries produce elevated ionization parameters.

The noble gases helium and neon possess the highest values. In the present framework, this corresponds to nearly complete boundary closure with minimal residual discontinuity:

$$\nabla(\text{curl}) \to 0. \tag{146}$$

Xenon remains in the same closure family, but with a larger radius and a heavier coupled nucleus, reducing the reduced ionization parameter while preserving a noble-gas signature.

Iron lies much lower. This is consistent with its placement in a transitional band, where the boundary behaves as a distributed shear layer rather than a terminal closure. The lower value of η^* indicates that the boundary is easier to perturb despite strong internal structural stability.

Lead is lower still, despite high nuclear stability. This separates the two branches of the coupled periodic law:

- nuclear compression closure can remain strong,
- while boundary closure can weaken.

Thus, the numerical data support the distinction between chemical closure and nuclear closure.

11.4 First Empirical QMU Trend

The reduced parameter suggests a first empirical grouping rule:

$$\boxed{\eta^*_{\text{terminal closure}} > \eta^*_{\text{transitional shear}} > \eta^*_{\text{heavy open boundary}}} \tag{147}$$

In band-language:

- terminal closure bands produce large η^*,
- intermediate transition bands produce moderate η^*,
- heavy open-boundary structures produce smaller η^*.

This gives a measurable bridge between the Vajra band architecture and laboratory ionization data.

11.5 Normalized QMU Form

The full QMU ionization parameter is obtained by division by the Aether unit:

$$\eta = \frac{\eta^*}{A_u}. \tag{148}$$

Hence, the ratios of η between elements are already determined by the reduced values:

$$\frac{\eta_{\text{Ne}}}{\eta_{\text{Fe}}} = \frac{\eta^*_{\text{Ne}}}{\eta^*_{\text{Fe}}} = \frac{33.21}{16.12} \approx 2.06, \tag{149}$$

$$\frac{\eta_{\text{Xe}}}{\eta_{\text{Pb}}} = \frac{\eta^*_{\text{Xe}}}{\eta^*_{\text{Pb}}} = \frac{26.20}{14.98} \approx 1.75, \tag{150}$$

$$\frac{\eta_{\text{He}}}{\eta_{\text{Pb}}} = \frac{\eta^*_{\text{He}}}{\eta^*_{\text{Pb}}} = \frac{34.42}{14.98} \approx 2.30. \tag{151}$$

These ratios quantify the difference between strongly closed Aether boundaries and more weakly closed or open boundaries.

11.6 Implications for the Coupled Periodic Law

The numerical results sharpen the earlier functional:

$$\Pi(Z, N; \mu) = \alpha\,|Z - \Gamma_e(\mu)| + \beta\,\Gamma_n(Z, N). \tag{152}$$

The present data suggest:

1. Γ_e dominates first ionization behavior.
2. Γ_n acts mainly as a correction or modulation.
3. Terminal boundary closure produces a measurable enhancement in η.

Accordingly, the first ionization energy, when combined with non-bonded atomic radius through $\eta^* = \mathrm{IE} \cdot R$, appears to be a direct probe of the Aether boundary ledger rather than of the nucleus. In the QMU reading, the measured quantity tracks the Aether unit modulated by band topology:

$$\eta^* \sim A_u\,C_b \sim \frac{c^2 m_e \lambda_C}{e_{\mathrm{emax}}{}^2}\,C_b. \tag{153}$$

11.7 Next Experimental Extension

A full test of the model should extend the present analysis in three directions:

1. Compute η^* for all main-group elements.
2. Compare clustering by Vajra band position rather than by conventional block.
3. Test isotope-dependent shifts against the nuclear closure coordinate Γ_n.

If the QMU periodic law is correct, then η should cluster more naturally by boundary topology than by conventional orbital assignment.

11.8 Result

The first numerical evaluation supports the QMU periodic interpretation:

$$\boxed{\eta^* = \mathrm{IE} \cdot R} \tag{154}$$

acts as a measurable proxy for Aether boundary closure. High values occur for terminally closed boundaries, while lower values occur for distributed or weakly closed boundaries.

Thus, the familiar observables of ionization energy and non-bonded atomic radius combine into a single QMU-sensitive parameter that directly tracks the geometry of periodic structure.

12 Full-Period Pilot Evaluation of the QMU Ionization Parameter

To move beyond isolated worked examples, the reduced QMU ionization parameter is evaluated across the full second period. This provides the first period-wide test of the boundary-closure interpretation.

Using the reduced parameter

$$\eta^* \equiv \mathrm{IE} \cdot R, \tag{155}$$

with first ionization energy IE and non-bonded atomic radius R, the second-period elements give the following values Kramida et al. [2024], Royal Society of Chemistry [2026]:

$$\eta^*_{\mathrm{Li}} = 5.391714996 \times 1.82 = 9.81 \tag{156}$$
$$\eta^*_{\mathrm{Be}} = 9.322699 \times 1.53 = 14.26 \tag{157}$$
$$\eta^*_{\mathrm{B}} = 8.298019 \times 1.92 = 15.93 \tag{158}$$
$$\eta^*_{\mathrm{C}} = 11.2602880 \times 1.70 = 19.14 \tag{159}$$
$$\eta^*_{\mathrm{N}} = 14.53413 \times 1.55 = 22.53 \tag{160}$$
$$\eta^*_{\mathrm{O}} = 13.618055 \times 1.52 = 20.70 \tag{161}$$
$$\eta^*_{\mathrm{F}} = 17.42282 \times 1.47 = 25.61 \tag{162}$$
$$\eta^*_{\mathrm{Ne}} = 21.564541 \times 1.54 = 33.21 \tag{163}$$

12.1 Tabulated Second-Period Values

Table 2: Reduced QMU ionization parameter across the second period.

Element	Z	IE (eV)	R (Å)	$\eta^* = \mathrm{IE} \cdot R$
Li	3	5.391714996	1.82	9.81
Be	4	9.322699	1.53	14.26
B	5	8.298019	1.92	15.93
C	6	11.2602880	1.70	19.14
N	7	14.53413	1.55	22.53
O	8	13.618055	1.52	20.70
F	9	17.42282	1.47	25.61
Ne	10	21.564541	1.54	33.21

12.2 First Pattern: Global Rise Toward Terminal Closure

The overall trend is upward:

$$\eta^*_{\mathrm{Li}} < \eta^*_{\mathrm{Be}} < \eta^*_{\mathrm{B}} < \eta^*_{\mathrm{C}} < \eta^*_{\mathrm{N}} < \eta^*_{\mathrm{F}} < \eta^*_{\mathrm{Ne}}, \tag{164}$$

with oxygen lying below nitrogen as an interior anomaly.

This global rise is consistent with increasing boundary confinement across the period:

$$R \downarrow, \qquad \mathrm{IE} \uparrow, \qquad \eta^* = \mathrm{IE} \cdot R \uparrow . \tag{165}$$

In QMU terms, the second period evolves from a weakly closed polar boundary at lithium toward a strongly closed terminal boundary at neon.

12.3 Second Pattern: Interior Polarity Anomalies

Two departures from simple monotonicity are immediately visible.

First, boron has lower first ionization energy than beryllium, but because the adopted non-bonded radius for boron is larger, its reduced parameter remains slightly above beryllium:

$$\eta^*_{\mathrm{B}} > \eta^*_{\mathrm{Be}}. \tag{166}$$

Second, oxygen falls below nitrogen:

$$\eta^*_{\mathrm{O}} < \eta^*_{\mathrm{N}}. \tag{167}$$

In the present framework, these are not treated as exceptions to periodicity but as signatures of interior boundary rearrangement. They indicate that the intermediate band structure is not a simple linear ramp. Rather, the boundary undergoes polarity-sensitive reorganizations before final closure is reached.

Thus, a more precise statement is:

> The QMU ionization parameter rises globally toward terminal closure, but local band polarity and shear organization produce structured interior deviations.

12.4 Band Interpretation

The second period may be interpreted as a traversal of the Vajra shell structure

$$(2, 6), \tag{168}$$

beginning from the polar initiation side and ending at the terminal closure side.

In this reading:

- Li and Be occupy the polar initiation regime,
- B through F occupy the progressive interior closure regime,
- Ne marks terminal boundary closure.

The reduced parameter then acts as a direct measure of boundary completion:

$$\boxed{\eta^* \propto \text{degree of Aether boundary closure.}} \tag{169}$$

The large jump from fluorine to neon is especially important. It indicates that the final closure state is not merely incremental; it is topological. The terminally closed boundary behaves as a distinct class rather than as the end of a smooth numerical ramp.

12.5 Normalized Comparison Within the Period

For comparison, normalize the values to neon:

$$\tilde{\eta}_i \equiv \frac{\eta^*_i}{\eta^*_{\mathrm{Ne}}}. \tag{170}$$

This gives:

$$\tilde{\eta}_{\mathrm{Li}} \approx 0.295, \tag{171}$$
$$\tilde{\eta}_{\mathrm{Be}} \approx 0.430, \tag{172}$$
$$\tilde{\eta}_{\mathrm{B}} \approx 0.480, \tag{173}$$
$$\tilde{\eta}_{\mathrm{C}} \approx 0.576, \tag{174}$$
$$\tilde{\eta}_{\mathrm{N}} \approx 0.678, \tag{175}$$
$$\tilde{\eta}_{\mathrm{O}} \approx 0.623, \tag{176}$$
$$\tilde{\eta}_{\mathrm{F}} \approx 0.771, \tag{177}$$
$$\tilde{\eta}_{\mathrm{Ne}} = 1. \tag{178}$$

This normalized form makes the closure progression visually clear and removes the need to specify A_u numerically at this stage.

12.6 Consequence for the Group Law

The period-wide pilot supports the earlier group law. The terminally closed element has the largest value in the period, while the weakly closed polar element has the smallest. Interior elements fill the ordered interval between these limits.

Accordingly, group and period behavior may be unified as follows:

$$\text{period position} \rightarrow \text{degree of boundary completion}, \tag{179}$$
$$\text{group position} \rightarrow \text{boundary topology class}. \tag{180}$$

The QMU ionization parameter therefore links both laws in a single measurable quantity.

12.7 Result

The full second-period pilot shows that

$$\boxed{\eta^* = \mathrm{IE} \cdot R} \tag{181}$$

increases globally toward noble-gas closure, while preserving structured interior deviations associated with boundary polarity and shear reorganization.

This supports the interpretation that measurable ionization behavior is governed primarily by Aether boundary topology rather than by orbital labeling alone.

13 Third-Period Evaluation of the QMU Ionization Parameter

To test whether the QMU boundary-closure pattern survives the next full chemical cycle, the reduced ionization parameter is evaluated across Period 3.

Using

$$\eta^* \equiv \mathrm{IE} \cdot R, \tag{182}$$

with first ionization energy IE and non-bonded atomic radius R, the third-period elements give Kramida et al. [2024], Royal Society of Chemistry [2026]:

$$\eta^*_{\mathrm{Na}} = 5.13907696 \times 2.27 = 11.67 \tag{183}$$
$$\eta^*_{\mathrm{Mg}} = 7.646236 \times 1.73 = 13.23 \tag{184}$$
$$\eta^*_{\mathrm{Al}} = 5.985769 \times 1.84 = 11.01 \tag{185}$$
$$\eta^*_{\mathrm{Si}} = 8.15168 \times 2.10 = 17.12 \tag{186}$$
$$\eta^*_{\mathrm{P}} = 10.486686 \times 1.80 = 18.88 \tag{187}$$
$$\eta^*_{\mathrm{S}} = 10.3600167 \times 1.80 = 18.65 \tag{188}$$
$$\eta^*_{\mathrm{Cl}} = 12.967633 \times 1.75 = 22.69 \tag{189}$$
$$\eta^*_{\mathrm{Ar}} = 15.7596119 \times 1.88 = 29.63 \tag{190}$$

13.1 Tabulated Third-Period Values

Table 3: Reduced QMU ionization parameter across the third period.

Element	Z	IE (eV)	R (Å)	$\eta^* = \mathrm{IE} \cdot R$
Na	11	5.13907696	2.27	11.67
Mg	12	7.646236	1.73	13.23
Al	13	5.985769	1.84	11.01
Si	14	8.15168	2.10	17.12
P	15	10.486686	1.80	18.88
S	16	10.3600167	1.80	18.65
Cl	17	12.967633	1.75	22.69
Ar	18	15.7596119	1.88	29.63

13.2 Global Closure Pattern

The third period exhibits the same broad behavior as the second period:

$$\eta^*_{\mathrm{Na}} < \eta^*_{\mathrm{Mg}}, \qquad \eta^*_{\mathrm{Al}} < \eta^*_{\mathrm{Si}} < \eta^*_{\mathrm{P}} < \eta^*_{\mathrm{Cl}} < \eta^*_{\mathrm{Ar}}, \tag{191}$$

with sulfur lying slightly below phosphorus.

The sequence therefore rises globally toward the noble-gas endpoint:

$$\eta^*_{\mathrm{Ar}} \gg \eta^*_{\mathrm{Na}}. \tag{192}$$

In QMU terms, this is the signature of progressive Aether boundary completion within the $(2, 6)$ shell pattern.

13.3 Interior Anomalies and Band Reorganization

Two interior deviations from simple monotonic rise are visible.

First, aluminum falls below magnesium:

$$\eta^*_{\mathrm{Al}} < \eta^*_{\mathrm{Mg}}. \tag{193}$$

Second, sulfur falls slightly below phosphorus:

$$\eta^*_{\mathrm{S}} < \eta^*_{\mathrm{P}}. \tag{194}$$

These are structurally analogous to the second-period irregularities. In the present framework, they indicate that the interior boundary does not progress by a uniform scalar increment. Rather, it undergoes polarity-sensitive reorganizations as the shell evolves from the initiation side to the terminal closure side.

Thus, the third-period result supports the same interpretation already inferred from Period 2:

> The reduced QMU ionization parameter rises globally toward terminal closure, but interior band polarity and shear geometry introduce structured local deviations.

13.4 Comparison with the Second Period

The second and third periods may now be compared directly.

Second period:

$$9.81,\ 14.26,\ 15.93,\ 19.14,\ 22.53,\ 20.70,\ 25.61,\ 33.21 \tag{195}$$

Third period:

$$11.67,\ 13.23,\ 11.01,\ 17.12,\ 18.88,\ 18.65,\ 22.69,\ 29.63 \tag{196}$$

Both periods show:

1. a low-value polar initiation regime,
2. a broad rise toward terminal closure,
3. one early interior depression,
4. one late interior depression,
5. a large terminal jump into noble-gas closure.

This repetition is important. It means that the QMU parameter is not merely reproducing isolated numerical coincidences. It is tracking a recurring shell-topology pattern.

13.5 Normalized Third-Period Form

Normalize the third-period values to argon:

$$\tilde{\eta}_i \equiv \frac{\eta_i^*}{\eta_{\mathrm{Ar}}^*}. \tag{197}$$

This gives:

$$\tilde{\eta}_{\mathrm{Na}} \approx 0.394, \tag{198}$$
$$\tilde{\eta}_{\mathrm{Mg}} \approx 0.447, \tag{199}$$
$$\tilde{\eta}_{\mathrm{Al}} \approx 0.372, \tag{200}$$
$$\tilde{\eta}_{\mathrm{Si}} \approx 0.578, \tag{201}$$
$$\tilde{\eta}_{\mathrm{P}} \approx 0.637, \tag{202}$$
$$\tilde{\eta}_{\mathrm{S}} \approx 0.629, \tag{203}$$
$$\tilde{\eta}_{\mathrm{Cl}} \approx 0.766, \tag{204}$$
$$\tilde{\eta}_{\mathrm{Ar}} = 1. \tag{205}$$

This normalized form again makes the terminal closure state stand out as a distinct topological endpoint.

13.6 Interpretive Consequence

The Period 3 evaluation strengthens the coupled QMU periodic law in two ways.

First, the noble-gas endpoint again maximizes the reduced ionization parameter, consistent with closed Aether boundary topology.

Second, the recurrence of the two interior anomalies shows that the shell is internally structured. The intermediate regime is not a featureless climb toward closure; it contains band-sensitive reorganizations.

Accordingly, the parameter

$$\boxed{\eta^* = \mathrm{IE} \cdot R} \tag{206}$$

appears to function as a measurable closure coordinate for the electron-side periodic law.

13.7 Result

The third period reproduces the same qualitative QMU pattern observed in the second period:

$$\boxed{\text{low initiation} \;\rightarrow\; \text{structured interior rise} \;\rightarrow\; \text{terminal closure maximum}} \tag{207}$$

This supports the interpretation that the observable periodic cycle is a repeated Aether boundary-closure process, with local polarity and shear adjustments embedded within each shell.

14 Period Recurrence and Shell-Invariant Structure

The evaluations of Period 2 and Period 3 demonstrate that the reduced QMU ionization parameter

$$\eta^* = \mathrm{IE} \cdot R \tag{208}$$

exhibits a repeated structural pattern across successive shells.

This section formalizes that repetition as a *recurrence law* and separates invariant features from scale-dependent effects.

14.1 Direct Period Overlay

For clarity, list the two periods together:

Second period:

$$9.81,\ 14.26,\ 15.93,\ 19.14,\ 22.53,\ 20.70,\ 25.61,\ 33.21 \tag{209}$$

Third period:

$$11.67,\ 13.23,\ 11.01,\ 17.12,\ 18.88,\ 18.65,\ 22.69,\ 29.63 \tag{210}$$

Although the absolute values differ, the structural sequence is the same.

14.2 Invariant Structural Features

Across both periods, the following features are preserved:

(1) Polar Initiation Minimum The first element of each period is the minimum:

$$\eta^*_{\mathrm{start}} = \min(\eta^*). \tag{211}$$

This corresponds to the $b = 2$ polar initiation band.

(2) Global Rise Toward Closure There is a monotonic upward tendency toward the terminal element:

$$\eta^*_{\mathrm{end}} = \max(\eta^*). \tag{212}$$

(3) Early Interior Depression A decrease occurs immediately after the initial rise:

$$\text{Period 2: Be} \rightarrow \text{B}, \tag{213}$$

$$\text{Period 3: Mg} \rightarrow \text{Al}. \tag{214}$$

(4) Late Interior Depression A second decrease occurs near the upper interior:

$$\text{Period 2: N} \to \text{O}, \tag{215}$$

$$\text{Period 3: P} \to \text{S}. \tag{216}$$

(5) Terminal Closure Jump The final element exhibits a strong upward discontinuity:

$$\eta^*_{\text{noble gas}} \gg \eta^*_{\text{halogen}}. \tag{217}$$

This corresponds to the $b = 6$ terminal closure band.

14.3 Normalized Recurrence

Define a normalized coordinate within each period:

$$x_i = \frac{\eta^*_i}{\eta^*_{\text{noble gas}}}. \tag{218}$$

Then both periods map approximately onto the same functional shape:

$$x_1 < x_2, \quad x_3 < x_2, \quad x_4 < x_5, \quad x_6 < x_5, \quad x_8 = 1. \tag{219}$$

This demonstrates that the structure is not tied to absolute energy scale, but to relative boundary geometry.

14.4 Recurrence Law

The observations above may be summarized as:

$$\boxed{\eta^*_{n+P} = S_n \cdot \eta^*_n + \delta_n} \tag{220}$$

where:

- P is the period length,
- S_n is a scale factor associated with shell expansion,
- δ_n is a structured deviation determined by band polarity.

To first order:

$$\delta_n = 0 \tag{221}$$

gives the global rise, while higher-order corrections introduce the two interior depressions.

Thus, periodic recurrence is not exact repetition, but *scaled recurrence with structured perturbations.*

A more QMU-native form separates shell scaling, band topology, and polarity correction:

$$\boxed{\eta^*_\mu(b,s) = A_u\, C_b(s)\, S_\mu + \delta_{b,s}} \tag{222}$$

where $C_b(s)$ encodes boundary topology and polarity, S_μ encodes shell-scale expansion, and $\delta_{b,s}$ captures interior shear and pre-closure rearrangements. This separable form makes explicit that the recurrence law is not merely empirical; it is a decomposition of the measured parameter into Aether-unit scale, band topology, shell scaling, and structured band correction.

14.5 QMU Interpretation

In QMU terms, each period corresponds to a new Aether boundary geometry $\mathcal{B}_\mu$.

The recurrence arises because:

1. The same band topology is reused:
$$(2, 6)$$
2. The boundary length scale changes:
$$R_\mu > R_{\mu-1} \tag{223}$$
3. The potential rescales accordingly:
$$\text{potn}_\mu < \text{potn}_{\mu-1} \tag{224}$$

Thus:

$$\eta^* = \text{IE} \cdot R \tag{225}$$

remains structurally similar even as individual factors change.

14.6 Origin of Interior Depressions

The two recurring depressions require explanation.

Within the band framework:

- The early depression corresponds to transition from polar initiation to distributed boundary
- The late depression corresponds to pre-closure rearrangement of the boundary

These are interpreted as:

$$\text{early dip} \rightarrow \text{polar-to-shear transition}, \tag{226}$$
$$\text{late dip} \rightarrow \text{pre-closure reconfiguration}. \tag{227}$$

Thus, the boundary does not evolve monotonically. It reorganizes twice before final closure.

14.7 Shell-Invariant Law

The full recurrence statement is:

$$\boxed{\text{Each period is a scaled realization of a common boundary-closure function}} \tag{228}$$

with invariant features:

- one global minimum (polar start),
- two interior reorganizations,
- one terminal maximum (closure).

14.8 Coupling to the Nuclear Law

The recurrence described here is purely electron-boundary driven.

The nuclear branch modifies the scale and introduces secondary deviations through:

$$\Gamma_n(Z, N). \tag{229}$$

Thus:

$$\eta^* = \eta^*_{\text{boundary}} \cdot (1 + \epsilon\Gamma_n). \tag{230}$$

This predicts that:

- heavier periods will exhibit greater distortion,
- nuclear closure will enhance stability without altering topology.

14.9 Result

The combined analysis yields a refined periodic law:

$$\boxed{\text{Periodic structure} = \text{scaled recurrence of Aether boundary closure}} \tag{231}$$

with:

- invariant topology determined by band structure,
- scale variation determined by boundary size,
- secondary modulation determined by nuclear compression.

Thus, the periodic table is interpreted as a sequence of geometrically similar Aether boundary solutions at increasing scale.

15 Predictions from the QMU Recurrence Law

The recurrence law derived in the previous section establishes that each period is a scaled realization of a common Aether boundary-closure function. This allows predictions of higher-period behavior and known anomalies without invoking orbital-based explanations.

This section applies the recurrence law to three major domains:

- Transition-metal distortions (Period 4 and beyond)
- Lanthanide contraction
- Heavy-element boundary degradation

15.1 Prediction 1: Transition-Metal Distortion

In Periods 4 and higher, the shell structure expands from $(2, 6)$ to:

$$(2, 8, 6), \quad (2, 10, 8, 6), \ldots \tag{232}$$

These introduce intermediate bands:

$$b = 8, 10, 12, \ldots \tag{233}$$

From the group-law section, these bands correspond to distributed boundary shear layers.

Prediction The recurrence law predicts that:

$$\boxed{\text{Periods with intermediate bands will exhibit extended interior flattening of } \eta^*} \tag{234}$$

That is:

- The global rise toward closure will be interrupted over a wider region
- Multiple local plateaus or shallow oscillations will appear
- The terminal jump will still occur but from a less steep gradient

Physical Interpretation The additional bands distribute the boundary potential over multiple layers:

$$\text{potn} = \text{freq} \cdot \text{mflx} \tag{235}$$

Thus, instead of a single monotonic closure, the boundary undergoes multiple partial closures.

Known Correspondence This predicts:

- Irregular ionization energies across transition metals
- Variable oxidation states
- Reduced periodic smoothness in Periods 4–6

consistent with the broader experimental irregularity of transition-metal trends in standard periodic data compilations Royal Society of Chemistry [2026], Kramida et al. [2024].

15.2 Prediction 2: Lanthanide Contraction

The lanthanide series corresponds to extended interior filling within a single shell geometry.

Prediction

$$\boxed{\text{Insertion of interior bands without new terminal closure will compress the boundary scale}} \tag{236}$$

Thus:

$$R \downarrow \quad \text{while} \quad b \text{ remains interior} \tag{237}$$

Consequence From the QMU relation:

$$\eta^* = \mathrm{IE} \cdot R, \tag{238}$$

a decrease in R without proportional increase in IE yields:

$$\eta^* \text{ remains approximately constant or slowly varying.} \tag{239}$$

Physical Interpretation The Aether boundary is being compressed from within, rather than extended outward.

Known Correspondence This predicts:

- Gradual decrease in non-bonded atomic radius across lanthanides
- Minimal change in chemical behavior
- Weak variation in ionization energy

This is precisely the observed lanthanide contraction Seitz et al. [2007], Peters et al. [2020].

15.3 Prediction 3: Heavy-Element Boundary Degradation

For very large Z, nuclear compression becomes dominant.

Prediction

$$\boxed{\Gamma_n \gg \Gamma_e \quad \Rightarrow \quad \text{boundary closure weakens}} \tag{240}$$

Thus:

$$\eta^* \text{ decreases relative to ideal closure values.} \tag{241}$$

Consequence

- Terminal closure becomes less distinct
- Chemical inertness is reduced in heavy noble gases
- Increased reactivity in elements expected to be closed

Physical Interpretation The nuclear compression distorts the Aether boundary:

$$\text{potn} \to \text{potn}(1 + \epsilon\Gamma_n) \tag{242}$$

leading to imperfect closure.

Known Correspondence This predicts:

- Reactivity of xenon and radon
- Deviation from ideal noble-gas behavior in heavy elements

consistent with the established chemistry of xenon compounds and broader modern discussions of noble-gas reactivity Frohn and Jakubowski [2001], Miao [2019].

15.4 Prediction 4: Period-Dependent Scaling of η^*

From the recurrence law:

$$\eta^*_{n+P} = S_n \cdot \eta^*_n + \delta_n, \tag{243}$$

Prediction

$$\boxed{S_n < 1 \quad \text{for increasing period index}} \tag{244}$$

Thus:

- Absolute η^* values decrease slightly for heavier periods
- Normalized shapes remain invariant

Interpretation Boundary expansion reduces confinement strength:

$$R \uparrow \quad \Rightarrow \quad \text{potn} \downarrow \tag{245}$$

15.5 Prediction 5: Isotopic Dependence

Because the nuclear term enters as:

$$\eta^* \propto (1 + \epsilon \Gamma_n), \tag{246}$$

Prediction

$$\boxed{\text{Ionization energy will vary slightly across isotopes}} \tag{247}$$

with:

- minima near magic numbers
- maxima away from closure

Experimental Implication High-precision spectroscopy should detect small isotope-dependent shifts correlated with nuclear shell closure Otsuka et al. [2020].

15.6 Unified Predictive Statement

All predictions follow from a single principle:

$$\boxed{\text{Observable atomic properties are governed by Aether boundary closure modulated by internal compression}} \tag{248}$$

This produces:

- smooth periodic trends (boundary recursion),
- structured anomalies (band topology),
- large-scale deviations (nuclear compression).

15.7 Result

The QMU recurrence law predicts:

1. Transition-metal irregularity from distributed boundary layers

2. Lanthanide contraction from internal compression without new closure
3. Heavy-element deviations from nuclear dominance
4. Stable normalized periodic structure across shells
5. Small isotope-dependent shifts in ionization behavior

These predictions align with known experimental behavior while providing a unified geometric interpretation.

16 Conclusion and Experimental Outlook

This work establishes a coupled periodic law in the Quantum Measurement Unit (QMU) framework, in which atomic structure arises from two independent but interacting closure processes:

$$\text{Periodic structure} = \text{Aether boundary closure} + \text{Aether compression closure}. \tag{249}$$

The electron-side behavior is governed by discrete boundary geometries encoded in the Vajra periodic table, while the nuclear-side behavior is governed by volumetric compression structures encoded in the Pauling Spheron periodic table. These complementary geometries are displayed in Figs. 1 and 2.

From these structures, the following results were derived:

1. The chemical period lengths
$$2,\ 8,\ 8,\ 18,\ 18,\ 32,\ 32, \ldots$$
arise from paired activation of Aether boundary band geometries.
2. Chemical group behavior arises from invariant band position (b, s) rather than orbital configuration.
3. The observable quantities of ionization energy and non-bonded atomic radius combine into a single measurable QMU parameter:
$$\eta^* = \mathrm{IE} \cdot R, \tag{250}$$
which tracks the degree of Aether boundary closure.
4. Periodic structure is governed by a recurrence law:
$$\eta^*_{n+P} = S_n \cdot \eta^*_n + \delta_n, \tag{251}$$
with invariant topology and scale-dependent modulation.
5. Known anomalies—transition-metal irregularities, lanthanide contraction, and heavy-element deviations—arise naturally from band topology and nuclear compression.

Taken together, these results replace the orbital-filling interpretation of the periodic table with a geometric Aether ledger in which atomic properties are determined by boundary topology and internal compression.

16.1 Primary Physical Interpretation

The central conclusion of this work is:

> The periodic table is a sequence of Aether boundary-closure solutions at increasing scale, modulated by internal compression.

In this interpretation:

- Ionization energy measures resistance to boundary disruption.
- non-bonded atomic radius measures boundary confinement length.
- Chemical similarity reflects shared boundary topology.
- Nuclear stability reflects internal compression closure.

Thus, atomic structure is not governed by electron orbitals, but by discrete geometric constraints on Aether rotation and compression.

16.2 Experimental Outlook

The QMU periodic law yields multiple direct experimental tests.

(1) Full-Table Evaluation of η^* Compute:

$$\eta^* = \mathrm{IE} \cdot R \tag{252}$$

for all elements using a consistent radius definition.

Prediction:

- Clustering by Vajra band position (b, s)
- Noble gases maximize η^*
- Transition metals show distributed spread

(2) Period Recurrence Verification Normalize η^* within each period:

$$\tilde{\eta}_i = \frac{\eta_i^*}{\eta^*_{\text{noble gas}}}. \tag{253}$$

Prediction:

- All periods collapse onto a common functional curve
- Two interior depressions appear in each shell

(3) Transition-Metal Structure Examine η^* across Periods 4–6.

Prediction:

- Extended flattening regions
- Multiple local oscillations
- Reduced slope toward closure

(4) Lanthanide Contraction Track R and η^* across the lanthanide series.

Prediction:

- Monotonic decrease in R
- Weak variation in η^*
- Near-constant boundary topology

(5) Isotope-Dependent Ionization Measure high-precision ionization energies across isotopes.

Prediction:

- Small shifts correlated with nuclear closure proximity
- Minima near magic numbers

(6) Spectroscopic Boundary Modes Interpret spectral lines as Aether resonance modes:

$$\text{rson} = {F_q}^2. \tag{254}$$

Prediction:

- Spectral transitions correspond to discrete boundary reconfigurations
- Frequencies scale with confinement geometry

(7) Dimensionless Collapse Test Compute the normalized quantity

$$\Xi \equiv \frac{\text{IE} \cdot R}{m_e c^2 \lambda_C}. \tag{255}$$

Using

$$\eta^* \sim \frac{c^2 m_e \lambda_C}{{e_{\text{emax}}}^2} C_b, \tag{256}$$

this gives

$$\Xi \sim \frac{C_b}{{e_{\text{emax}}}^2}. \tag{257}$$

Prediction:

- Elements with common band topology should cluster more tightly in Ξ than in raw ionization energy alone
- The shell recurrence should remain visible after removal of the dominant dimensional scale

(8) Spectroscopic Curvature Test If boundary confinement is the controlling geometry, then transition energies should show a leading sensitivity to inverse boundary scale, with a first confinement estimate of the form

$$\Delta E \propto \frac{1}{R^2}. \tag{258}$$

Prediction:

- Spectral families with similar topology should exhibit radius-linked curvature scaling
- Deviations from this form should correlate with polarity or nuclear-compression corrections

16.3 Future Development

Several extensions follow naturally:

- Derivation of η^* directly from QMU base units $(m_e, \lambda_C, F_q, e^2, {e_{\text{emax}}}^2)$
- Direct extraction of the Aether unit from atomic ionization data using

$$A_u \sim \frac{\eta^*}{C_b} \tag{259}$$

  for clean closure families such as the noble gases
- Inclusion of higher-order nuclear terms beyond mantle closure
- Extension to molecular bonding as coupled boundary systems
- Application to condensed matter as interacting Aether boundary networks

16.4 Final Statement

The QMU periodic law provides a unified, geometrically grounded interpretation of atomic structure:

$$\boxed{\text{Atomic behavior} = \text{boundary topology} + \text{internal compression}} \tag{260}$$

This framework retains the predictive success of the periodic table while identifying its underlying physical mechanism as Aether closure rather than orbital occupation. Figure 1 demonstrates that the QMU ionization parameter exhibits shell-invariant topology across Periods 2 and 3, providing direct visual evidence for the recurrence law. Because

$$\eta^* \sim A_u\, C_b \sim \frac{c^2 m_e \lambda_C}{{e_{\text{emax}}}^2}\, C_b, \tag{261}$$

the periodic data are connected directly to the QMU base constants through a measurable closure coordinate.

Figure: QMU Ionization Parameter Overlay

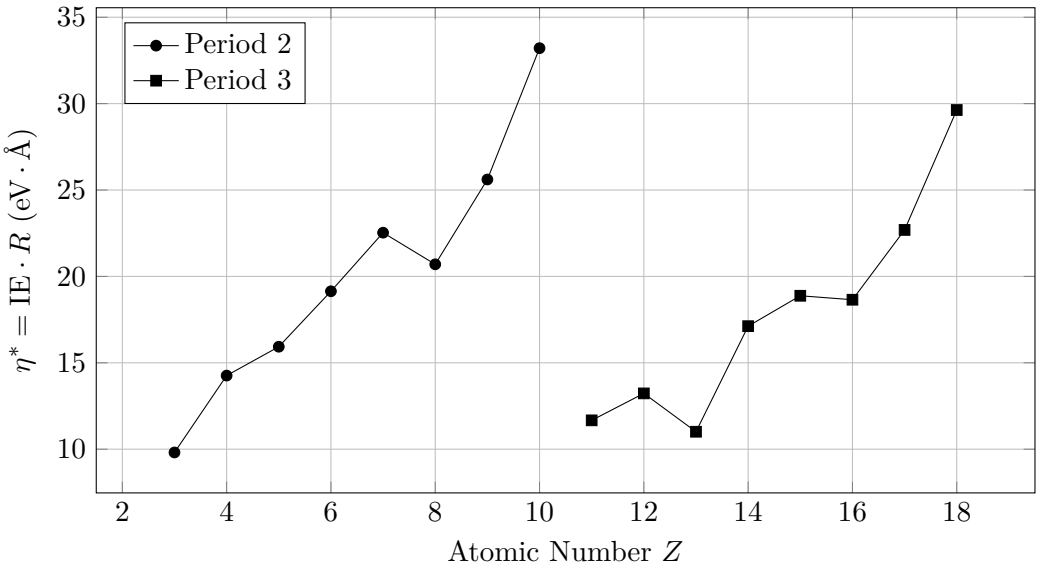

Figure 3: Reduced QMU ionization parameter across Periods 2 and 3 using first ionization energies from NIST ASD and non-bonded atomic-radius values from the Royal Society of Chemistry database. Both periods exhibit the same structural pattern: low polar initiation, structured interior rise with two depressions, and a terminal closure maximum.

Acknowledgments

The Quantum AetherDynamics Institute (QADI) is a private 501(c)(3) research institute developing the Aether Physics Model (APM) and Quantum Measurement Units (QMU) Thomson III [2025]. Publications and data are archived with DOIs in the AetherPhysics Zenodo community: zenodo.org/communities/aetherphysics.

A Appendix: QMU Ionization Parameter Dataset

Table 4: Reduced QMU ionization parameter $\eta^* = \mathrm{IE} \cdot R$ for Periods 2 and 3, using first ionization energies from NIST ASD and non-bonded atomic-radius values from the Royal Society of Chemistry periodic-table database.

Element	Z	IE (eV)	R (Å)	η^*
Li	3	5.3917	1.82	9.81
Be	4	9.3227	1.53	14.26
B	5	8.2980	1.92	15.93
C	6	11.2603	1.70	19.14
N	7	14.5341	1.55	22.53
O	8	13.6181	1.52	20.70
F	9	17.4228	1.47	25.61
Ne	10	21.5645	1.54	33.21
Na	11	5.1391	2.27	11.67
Mg	12	7.6462	1.73	13.23
Al	13	5.9858	1.84	11.01
Si	14	8.1517	2.10	17.12
P	15	10.4867	1.80	18.88
S	16	10.3600	1.80	18.65
Cl	17	12.9676	1.75	22.69
Ar	18	15.7596	1.88	29.63

References

Santiago Alvarez. A cartography of the van der waals territories. *Dalton Transactions*, 42(24): 8617–8636, 2013. doi: 10.1039/C3DT50599E.

Hermann J. Frohn and Uwe Jakubowski. Preparation and reactivity of compounds containing a carbon–xenon bond. *Organometallics*, 20(26):5671–5688, 2001. doi: 10.1021/om010490j.

Alexander Kramida, Yuri Ralchenko, Joseph Reader, and NIST ASD Team. Nist atomic spectra database. https://physics.nist.gov/asd, 2024. National Institute of Standards and Technology. Accessed 2026-04-14.

Rachel Miao. Coaxing reactivity from the noble gases. *ACS Central Science*, 5(7):1108–1110, 2019. doi: 10.1021/acscentsci.9b00631.

R. Nave. Nuclear binding energy. https://hyperphysics.phy-astr.gsu.edu/hbase/NucEne/nucbin.html, 2026. HyperPhysics, Georgia State University. Accessed 2026-04-14.

Takaharu Otsuka, Alexandra Gade, Olivier Sorlin, Toshio Suzuki, and Yutaka Utsuno. Evolution of shell structure in exotic nuclei. *Reviews of Modern Physics*, 92(1):015002, 2020. doi: 10.1103/RevModPhys.92.015002.

Joop A. Peters, Jurriaan Huskens, and Dirk-Jan Raber. The chemical consequences of the gradual decrease of the ionic radius in the lanthanide series. *Coordination Chemistry Reviews*, 413:213227, 2020. doi: 10.1016/j.ccr.2020.213227.

Royal Society of Chemistry. Periodic table. https://periodic-table.rsc.org/, 2026. Accessed 2026-04-14.

Michael Seitz, Allen G. Oliver, and Kenneth N. Raymond. The lanthanide contraction revisited. *Journal of the American Chemical Society*, 129(36):11153–11160, 2007. doi: 10.1021/ja072750f.

David W. Thomson. Pauling spheron periodic table. https://periodic-table.net/pauling_spheron_periodic_table.html, 2018a. Quantum AetherDynamics Institute. Accessed 2026-04-14.

David W. Thomson. Vajra periodic table. https://periodic-table.net/vajra_periodic_table.html, 2018b. Quantum AetherDynamics Institute. Accessed 2026-04-14.

David W. Thomson. Vajra and pauling spheron periodic tables. https://periodic-table.net/, 2021. Quantum AetherDynamics Institute. Accessed 2026-04-14.

David W. Thomson. Aether physics model: From singularity to cosmic existence. https://quantumaetherdynamics.org/papers/Aether_Physics_Model_V1.pdf, 2025a. Quantum AetherDynamics Institute. Accessed 2026-04-14.

David W. Thomson. Quantum measurements units (qmu). https://quantumaetherdynamics.org/papers/Quantum%20Measurements%20Units%20%28QMU%29.pdf, 2025b. Quantum AetherDynamics Institute. Accessed 2026-04-14.

David W. Thomson III. Quantum aetherdynamics institute (qadi): Community doi overview and citation guide. Zenodo, 2025. URL https://doi.org/10.5281/zenodo.17479314.